

See discussions, stats, and author profiles for this publication at: <https://www.researchgate.net/publication/329948848>

Aerodynamic Force Modeling of Multirotor Unmanned Aerial Vehicles

Article in *AIAA Journal* · December 2018

DOI: 10.2514/1.1057165

CITATIONS

29

READS

1,012

5 authors, including:



Jérémie Xavier Joseph Bannwarth
Seachange New Zealand Limited

7 PUBLICATIONS 72 CITATIONS

[SEE PROFILE](#)



Zhenrong Jeremy Chen
University of Auckland

10 PUBLICATIONS 198 CITATIONS

[SEE PROFILE](#)



Karl Alexander Stol
University of Auckland

116 PUBLICATIONS 3,022 CITATIONS

[SEE PROFILE](#)



Bruce Macdonald
University of Auckland

228 PUBLICATIONS 7,429 CITATIONS

[SEE PROFILE](#)

Aerodynamic Force Modeling of Multirotor Unmanned Aerial Vehicles

Jérémie X. J. Bannwarth,* Z. Jeremy Chen,† Karl A. Stol,‡ Bruce A. MacDonald,§
and Peter J. Richards¶

University of Auckland, Auckland 1010, New Zealand

DOI: 10.2514/1.J057165

This paper describes a novel multirotor unmanned aerial vehicle aerodynamic force model with the aim of creating a multirotor simulation that is suitable for the evaluation of station-keeping performance in turbulent wind. It fills the gap between simple models that ignore important aerodynamic effects and other more comprehensive but computationally expensive models. The model is synthesized from static wind tunnel test data and accounts for variations in angular rotor speed, apparent wind speed, and angle of attack on the vehicle's rotors. Experimental validation is performed through indoor free-flight pitch step responses. On average, the simulated root mean square pitch tracking error is found to be within 31% of the experiment. The usefulness of the whole system to determine station-keeping performance is assessed by free-flight station-keeping experiments in a wind tunnel environment. The tracking error along all three axes is found to increase with increasing mean wind speed. The simulated standard deviation of errors along the wind direction is on average within 7% of the experiment, whereas those of the errors along axes perpendicular to the wind direction are found to be within 56%. Overall trends are similar in all cases, making the model suitable for performance comparisons of flight controllers.

Nomenclature

A_{prop}	=	representative area of propeller, m^2
A_{UAV}	=	representative area of UAV, m^2
b	=	rotor drag coefficient, $(\text{kg} \cdot \text{m}^2)/\text{rad}^2$
D_{prop}	=	diameter of propeller, m
D_{UAV}	=	rotor-to-rotor diameter of UAV, m
${}^B\mathbf{F}_{\text{aero}}$	=	total aerodynamic force vector acting on UAV, N
\mathbf{G}	=	gravity force vector, N
\mathbf{I}	=	inertia tensor of the UAV, $\text{kg} \cdot \text{m}^2$
$I_{R,zz}$	=	rotor mass moment of inertia about its axis, $\text{kg} \cdot \text{m}^2$
${}^B\mathbf{M}_{\text{aero}}$	=	total aerodynamic moment vector acting on UAV, $\text{N} \cdot \text{m}$
m_t	=	total UAV mass, kg
N	=	number of rotors of the UAV
\mathbf{R}_B	=	transformation matrix from body to world frame
${}^B\mathbf{T}$	=	total rotor force vector, N
${}^B\mathbf{T}_i$	=	force vector generated by rotor i , N
$T_{i,xy}$	=	transverse force generated by rotor i , N
$T_{i,z}$	=	axial force generated by rotor i , N
\mathbf{U}	=	wind vector in world frame, m/s
${}^B\mathbf{U}_{\text{app}}$	=	apparent wind speed vector on UAV, m/s
${}^B\mathbf{V}$	=	UAV linear velocity vector in body frame, m/s
α	=	angle of attack of wind on UAV, rad
β	=	sideslip angle of wind on UAV, rad
ϕ, θ, ψ	=	roll, pitch, and yaw angles of the UAV, rad

λ_i	=	tip speed ratio of rotor i
${}^B\mathbf{V}$	=	UAV angular velocity vector in body frame, rad/s
ρ	=	air density, kg/m^3
${}^B\boldsymbol{\tau}$	=	total rotor torque vector, $\text{N} \cdot \text{m}$
${}^B\boldsymbol{\tau}_i$	=	torque vector generated by rotor i , $\text{N} \cdot \text{m}$
ω_i	=	angular speed of rotor i , rad/s

Superscript

B	=	in body frame
-----	---	---------------

I. Introduction

THE use of unmanned aerial vehicles (UAVs) has increased drastically in recent years. They started mostly as mobile photography platforms for applications such as remote surveying, where accurate position keeping performance is not crucial and interactions with the environment are not primary concerns. However, UAVs are used increasingly for applications close to the environment such as foliage sampling [1], inspection of buildings [2], and spraying of weeds [3]. Such applications require a higher level of accuracy due to risks of collision with the environment and the influence of station-keeping performance on the quality of the work being performed. Furthermore, the use of UAVs in increasingly difficult flight conditions is becoming a focus for applications such as filming, search and rescue, and inspections.

Wind disturbance rejection is an important aspect of drone aerodynamics as steady wind disturbances limit the range of operation of UAVs, and unsteady wind disturbances degrade their performance and stability [4]. This results in a loss of revenue and, in extreme cases, prevents the completion of the desired work. Understanding how disturbances affect the plant allows to develop better simulation models and controllers to predict and mitigate their effects, respectively.

Accurate simulation models enable quick, safe, and cost-effective investigation of UAV performance and are a big asset to the UAV development process. However, the modeling of aerodynamic forces for multirotor UAVs remains an underdeveloped area of research. Because of the complexity of aerodynamic effects, past work has usually relied on simple UAV models where the aerodynamic forces and moments are either ignored entirely [5,6], or where the moments applied on the UAV are calculated as being proportional to the square of its angular velocities and where aerodynamic forces are omitted entirely [7,8]. This is acceptable for low-velocity operations in low-wind-speed conditions. However, higher apparent wind speeds result

Received 4 March 2018; revision received 29 September 2018; accepted for publication 17 October 2018; published online 24 December 2018. Copyright © 2018 by Jérémie X. J. Bannwarth, Z. Jeremy Chen, Karl A. Stol, Bruce A. MacDonald, and Peter J. Richards. Published by the American Institute of Aeronautics and Astronautics, Inc., with permission. All requests for copying and permission to reprint should be submitted to CCC at www.copyright.com; employ the ISSN 0001-1452 (print) or 1533-385X (online) to initiate your request. See also AIAA Rights and Permissions www.aiaa.org/randp.

*Ph.D. Candidate, Department of Mechanical Engineering; jban039@aucklanduni.ac.nz.

†Research Fellow, Department of Mechanical Engineering; zhenrong.chen@auckland.ac.nz.

‡Senior Lecturer, Department of Mechanical Engineering; k.stol@auckland.ac.nz.

§Professor, Department of Electrical and Computer Engineering; b.macdonald@auckland.ac.nz.

¶Associate Professor, Department of Mechanical Engineering; pj.richards@auckland.ac.nz.

in the generation of significant aerodynamic forces and moments that are not adequately modeled by these simple models. Some research accounts for aerodynamic forces by including a force disturbance in their equations of motion that represents exogenous inputs such as the force generated by constant wind [9]. Other research models the aerodynamic forces as a vector acting in the same direction as the applied wind vector with a magnitude proportional to that of the square of the magnitude of the said applied wind vector [10]. However, the effects of the inflow angle of the applied wind vector and rotor speed on aerodynamic forces are not usually taken into account, despite the potential significance of these effects.

Some research on the aerodynamics of individual rotors is available. Månsson and Stenberg [11] obtain model parameters for an individual rotor model using a computer-assisted design (CAD) model. These parameters are then adjusted based on experimental data obtained from static testing of an individual rotor in a wind tunnel. However, the authors validate the rotor model only for axial flight. In addition, the authors model the airframe drag forces separately and note that the validity of their airframe model is relatively poor. Other work includes the testing rig developed by Ramasamy [12] to measure thrust and torque for single, coaxial, and tilted rotors. He presents a series of experiments to investigate the effects of different rotor arrangements and rotor parameters such as number of blades on performance, including output thrust, torque, and power. However, this research does not investigate other forces and moments generated by the rotors. On a similar topic, Yoon et al. [13] present a computational fluid dynamics (CFD) model of a full UAV based on three-dimensional Navier-Stokes equations to investigate the effects of torque balancing on the performance of coaxial rotor systems. Their results show good correlation with experimental results from Ramasamy [12]. CFD models provide insight into the flow dynamics that is especially useful in cases where there is a risk of interaction either between different rotors or with the wind. However, such models are complex to develop and computationally intensive.

Theys et al. [14] also present wind tunnel testing results for individual rotors. They investigate how the coefficients of their drag and moment models vary over three different wind speeds (0, 6, and 9 m/s), a wide range of rotor speeds, and various rotor angles with respect to the wind direction. Because of the coarse 30° increments in inflow angles used, the results are fairly limited for use in simulations of hover in windy conditions, where the pitch angle of the UAV is expected to remain within roughly $\pm 45^\circ$ from the horizontal. However, the results highlight interesting trends. Of special interest is the increasing pitching moment generated by the rotor as the wind speed is increased and the wind vector moves closer to normal from the rotor axis. The magnitude of this moment is similar to that of the primary moment generated around the rotor axis. This effect is not modeled in usual aerodynamic models even though it has the potential of affecting performance at higher wind speeds.

Khan and Nahon [15] present an analytical rotor model for general forward flight conditions and validate their model against data from Theys et al. [14]. Their model is based on well-established blade element momentum theory and is combined with an inflow model from existing literature. They comprehensively explore the different aerodynamic effects that affect the rotor. Their model matches well with experimental results for the primary force and moment along the rotor axes. On the other hand, the accuracy of the secondary moments degrades when the incident angle of the wind rotates away from the axis of the rotor. However, the same general trends presented by Theys et al. [14] remain; the secondary moments are similar in magnitude to the primary moment, and it is thus necessary to account for them in a high-fidelity model. The model presented also necessitates measuring rotor dimensions accurately. The same research group applies their rotor model for quadcopter control in a wind field [16]. The blade element theory model is computationally intensive and is therefore used offline to generate a look-up table that enables real-time simulation. The UAV model uses a simplified approach to model the wake interference occurring when one rotor is behind another one with respect to the wind. Luo et al. [17] present a quadcopter interference model derived from theory. The model is validated in simulation using CFD, showing a reasonably good fit, but no experimental validation is presented.

Much of the research to date has been focused on the development of models and testing of components, but there is a lack of free-flight experimental testing. This is likely due to the difficulty and expense associated with such experimental testing; outdoor testing is not easily repeatable due to the variability of the wind, whereas indoor testing requires large facilities. Reliably generating appropriate flow conditions indoors is a further issue. Some research [9,18–20] has described the use large fans to generate a wind disturbance. However, this is a rather coarse method of doing so with little room for adjustment. Performing flight tests in a wind tunnel provides more control over the wind characteristics. Lee and Han [21] present a magnetic suspension and balance system for testing micro-UAVs in a wind tunnel. In addition, Smeur et al. [22] assessed the gust disturbance rejection performance of their controller by flying a small 0.4 kg Parrot Bebop quadcopter in and out of a wind tunnel's jet. On the other hand, wind tunnels have been scantily used for flight testing larger multirotor UAVs. This paper presents a new UAV model with the aim of assessing hover controller performance in windy flight conditions. It models aerodynamic effects that are important at higher speeds but are usually ignored in models to date. Section II describes the quaternion-based UAV model used, and Sec. III presents aerodynamic force models and the static wind drag measurement experiments used to develop them. Section IV describes free-flight pitch response experiments used to validate the aerodynamic moment model, and Sec. V describes the free-flight hover experiments used to validate the complete model and assess its ability to predict hover performance. Finally, conclusions and future work are described in Sec. VI.

II. Modeling

This section covers the modeling of a multirotor UAV. It defines the notation used throughout the paper and provides context for the drag and lift models that are obtained by fitting experimental data in Sec. III. The UAV model uses quaternion-based equations of motion derived from first principles.

A. Assumptions

All components of the UAV are assumed to be rigid bodies. Both the UAV and its motors are assumed to be symmetrical about their principal axes. Unless otherwise stated, their inertia tensors are diagonal. Furthermore, for the purpose of force calculations, the UAV is assumed to be rotationally symmetric about its z axis. This means that the magnitude of the drag force applied on the UAV is only affected by the magnitude and angle of the apparent wind vector. The sideslip of the relative velocity is assumed to have no effect on the magnitude of the drag produced. This assumption is made in order to reduce the complexity of the aerodynamic model fitting process presented in Sec. III and reduce the number of experimental data samples required.

B. Reference Frames and Coordinate Transforms

Figure 1 shows the reference frames used. Unless explicitly denoted with the \mathcal{B} superscript, vectors are assumed to be expressed

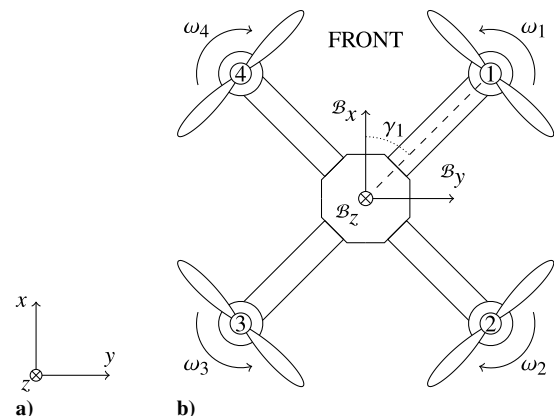


Fig. 1 Top-down view of the reference frames used. a) Inertial frame \mathcal{O} ; b) body frame \mathcal{B} .

in the inertial frame. As can be seen, the inertial and body frames adopt the typical north-east-down (NED) convention. The forward axis of the quadcopter is coincident with Bx .

The UAV's position in the world frame is expressed as $\xi = [x \ y \ z]^T$, while its orientation is expressed as the quaternion q . The orientation can also be expressed in terms of its Euler angles; $\eta = [\phi \ \theta \ \psi]^T$. ϕ , θ , and ψ represent the roll, pitch, and yaw angles of the UAV, respectively. $^B\mathbf{V} = [^Bv_x \ ^Bv_y \ ^Bv_z]^T$ and $^B\boldsymbol{\nu} = [^B\omega_p \ ^B\omega_q \ ^B\omega_r]^T$ represent the UAV's linear and angular velocities, respectively. The transformation matrix from the body frame B to the world frame \mathcal{O} is defined as \mathbf{R}_B , yielding

$$\dot{\xi} = \mathbf{R}_B ^B\mathbf{V} \quad (1)$$

C. Equations of Motion

The UAV's equations of motion are expressed as Eqs. (2) and (3), consistent with the standard form for aircraft dynamics [7].

$$^B\dot{\mathbf{V}} = \frac{1}{m_t} (\mathbf{R}_B^T \mathbf{G} + ^B\mathbf{T} - ^B\boldsymbol{\nu} \times m_t ^B\mathbf{V} + ^B\mathbf{F}_{\text{aero}}) \quad (2)$$

$$^B\dot{\boldsymbol{\nu}} = \mathbf{I}^{-1} (^B\boldsymbol{\tau} - ^B\boldsymbol{\nu} \times (\mathbf{I}^B \boldsymbol{\nu}) + ^B\mathbf{M}_{\text{aero}}) \quad (3)$$

$\mathbf{G} = [0 \ 0 \ 9.81m_t]^T$ represents the gravity vector. $^B\mathbf{T}$ and $^B\boldsymbol{\tau}$ represent the total thrust force and torque applied by the UAV's motors. Likewise, $^B\mathbf{F}_{\text{aero}}$ and $^B\mathbf{M}_{\text{aero}}$ represent the total aerodynamic force and moment acting on the aircraft. m_t and \mathbf{I} represent the UAV's total mass and inertia tensor, respectively.

D. Aerodynamics

All aerodynamic computations are performed in the body frame. A free body diagram of the forces acting on the UAV is shown in Fig. 2. $^B\mathbf{U}_{\text{app}}$ represents the apparent wind speed on the UAV accounting for the relative motion of the UAV in space. It is defined as

$$^B\mathbf{U}_{\text{app}} = -(^B\mathbf{V} + \mathbf{R}_B^T \mathbf{U}) \quad (4)$$

The angles between $^B\mathbf{U}_{\text{app}}$ and the $^Bx^By$ and $^Bx^Bz$ planes are referred to as the angle of attack, α , and the sideslip angle, β , respectively.

The aerodynamic forces acting on the UAV are assumed to act solely within the plane spanned by $^B\mathbf{U}_{\text{app}}$ and Bz . $^B\mathbf{F}_{\text{aero}}$ represents the aerodynamic force vector acting about the center of mass and $^B\mathbf{T}_i$ represents the thrust-inclusive force vector acting about rotor i . $^B\mathbf{M}_{\text{aero}}$ represents the aerodynamic moment acting about the UAV's center of mass.

E. Rotor Dynamics

The total force and moment applied by the motors on the UAV, including gyroscopic effects, are expressed as

$$^B\mathbf{T} = \sum_{i=1}^N ^B\mathbf{T}_i = \sum_{i=1}^N \begin{bmatrix} -T_{i_{xy}} \cos(\beta) & -T_{i_{xy}} \sin(\beta) & -T_{i_z} \end{bmatrix}^T \quad (5)$$

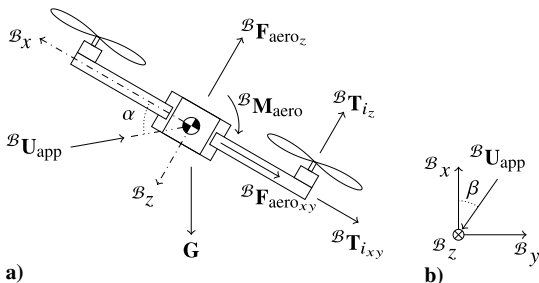


Fig. 2 Free body diagram of the UAV. a) Side view for $\beta = 0$; b) plan view.

$$^B\boldsymbol{\tau} = \sum_{i=1}^N (^B\boldsymbol{\tau}_i - ^B\boldsymbol{\nu} \times (\mathbf{I}_R \boldsymbol{\omega}_i)) \quad (6)$$

where N represents the number of rotors and \mathbf{I}_R is the rotor's inertia tensor. As shown in Fig. 2a, $T_{i_{xy}}$ and T_{i_z} are functions representing the thrust and aerodynamic forces generated by rotor i and are developed through experimental testing in Sec. III. Similarly, $^B\boldsymbol{\tau}_i$ represents the moment generated by rotor i and is defined as

$$^B\boldsymbol{\tau}_i = [0 \ 0 \ -b\omega_i^2 - I_{R,zz}\dot{\omega}_i]^T + \mathbf{L}_i ^B\mathbf{T}_i \quad (7)$$

where b is the rotor drag coefficient, $I_{R,zz}$ is the mass moment of inertia of the rotor about its axis, and

$$\mathbf{L}_i = \frac{1}{2} D_{\text{UAV}} \begin{bmatrix} 0 & 0 & \sin(\gamma_i) \\ 0 & 0 & -\cos(\gamma_i) \\ -\sin(\gamma_i) & \cos(\gamma_i) & 0 \end{bmatrix} \quad (8)$$

γ_i represents the counterclockwise angle between the positive Bx axis and a line going from the center of the UAV to the center of rotor i , as shown in Fig. 1. D_{UAV} is the distance between opposite rotors, such as rotors 1 and 3 in Fig. 1.

III. Static Aerodynamic Experiment

This section describes the experiment conducted to measure the aerodynamic forces generated on a typical UAV for varying combinations of wind speed, angle of attack, and mean rotor speed.

A. Experimental Setup

Figure 3 shows a picture of the experimental setup used. The UAV used for this experiment has a mass of approximately 1.5 kg, has a diagonal distance between opposite rotors of 0.45 m, and is built using off-the-shelf parts. Its frame has the same geometry as the DJI Flame Wheel [23], which is commonly used for hobby and laboratory research applications. The propellers used are RCTIMER CFN1045. They are made up of carbon fiber and have a diameter of 0.25 m and a pitch of 0.11 m. The UAV was mounted on a rig and placed in the wind tunnel setup developed in [24] with the aim of measuring the aerodynamic forces acting on the UAV under a range of different wind speeds, angles of attack, and rotor speeds.

A JR3 load cell, model number 160M50A4, was chosen to measure resulting forces and moments. The sensor has an accuracy of $\pm 0.25\%$. It has maximum ratings of 400 N, 80 N, and $12.5 \text{ N} \cdot \text{m}$ for axial, transverse, and angular loadings. The sensor was mounted on an adjustable clamp, enabling the angle of attack of the wind to be varied from 5° (UAV pitched nose up) to -45° (UAV pitched nose down into the wind). The vertical distance from the center of the sensor to the center of mass of the UAV was measured to be 0.185 m. The wind tunnel is of the open jet type with a height of 3.5 m and a width that can be adjusted from 2.5 to 7 m. For this part of the testing the width was set to 2.5 m. As described in Sec. V, the nominal flight

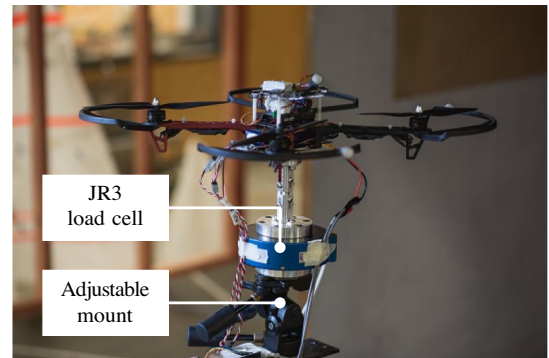


Fig. 3 Experimental setup for static drag and thrust measurements.

location for free-flight operation was chosen to be in the center of the jet, 2.5 m from the jet exit, and 1.5 m above the tunnel floor to ensure safe operation. The rig was arbitrarily placed in the same location for the purpose of this static test.

B. Testing Procedure

First, the angle of attack of the wind, α , was varied from 5° to -45° in 5° steps. For each pitch angle, the wind tunnel speed setting was incrementally increased, yielding wind speeds of $\{0, 3.1, 6.6, 10.1, 13.7\}$ m/s. For each combination of pitch and wind speed, measurements were taken while the motors were at rest. Subsequently, the pulse width sent to the motors was varied from 10 to 90% in 5 equally spaced increments, yielding rotational speeds of $\omega = \{224, 383, 543, 702, 861\}$ rad/s. An RPM sensor was used to compare the rotational speed of one of the motors under varying combinations of wind speed and tilt angle, but no significant changes were observed. As a point of comparison, on a full battery the UAV hovers halfway through the PWM range, which corresponds to a reference rotational speed of approximately 540 rad/s. For each test case, the force and torque responses around the x , y , and z axes of the sensor were recorded and averaged over a period of 5 s. To remove the effect of gravity on the measurements, for each α , the offsets measured at zero wind speed and zero rotor speed were subtracted from the rest of the data.

C. Results and Discussion

The models presented in this section were chosen empirically to best match the experimental results. All coefficients were made dimensionless through dimensional analysis in an attempt to generalize the models presented. First, models for the axial component of the aerodynamic force, $^B F_{\text{aero}}$, and the axial component of the force generated by rotor i , $^B T_i$, presented in Fig. 2, were chosen as

$$F_{\text{aero}_z} = \frac{1}{2} \rho U^2 C_{z,1}(\alpha) A_{\text{UAV}} \quad (9)$$

$$T_{i_z} = \frac{1}{2} \rho \omega_i^2 C_{z,2} D_{\text{prop}}^2 A_{\text{prop}} + \frac{1}{2} \rho C_{z,3}(\alpha, \lambda_i) U \omega_i D_{\text{prop}} A_{\text{prop}} \quad (10)$$

where ρ is the density of air and $A_{\text{UAV}} = \pi D_{\text{UAV}}^2/4$ is a representative area for the UAV, arbitrarily chosen to be a disc. Likewise, D_{prop} is the diameter of the rotors and $A_{\text{prop}} = \pi D_{\text{prop}}^2/4$. $C_{z,1}$, $C_{z,2}$, and $C_{z,3}$ are dimensionless aerodynamic coefficients. The first term of T_{i_z} is proportional to the square of the rotor speed and corresponds to a widely used thrust model in the UAV literature. The second term is proportional to the product of the rotor speed and wind speed. It was added based on insight into the recorded data in order to account for observed variations in axial rotor force. While the models presented here are intended for use within the range of tested parameters, the models for the coefficients were chosen to be valid for angles of attack ranging from -180° to 180° for ease of linearization and simulation. A three-step procedure was followed to fit these models. In the absence of wind, F_{aero_z} and the second component of T_{i_z} are zero. In addition, the UAV used has four rotors, which are all assumed to produce identical forces as interference is not modeled. As a consequence, $C_{z,2}$ was first fitted to a quarter of the z -axis force measured at zero wind speed using least squares regression, yielding

$$C_{z,2} = 5.13 \times 10^{-3} \quad (11)$$

Figure 4a compares the thrust force predicted by the model to that recorded in the experiment. An accurate match can be observed, showing the accuracy of this widely used rotor thrust model in the absence of wind.

Making use of the computed value of $C_{z,2}$, the forces generated by the four rotors due to the first term of T_{i_z} were then summed up and subtracted from all the recorded z -axis force measurements. At zero rotor speed, the rotors are not expected to produce any axial force,

which means that the only axial force acting on the body is F_{aero_z} . The body aerodynamic force coefficient $C_{z,1}$ was thus computed for all the data points recorded at zero rotor speed. The function used to compute $C_{z,1}$ has to be even about $\alpha = 90^\circ, -90^\circ$ as the UAV is assumed to be symmetric about its $^B x^B z$ and $^B y^B z$ planes. A sinusoidal-based function was empirically chosen and fitted to the computed coefficients, yielding

$$C_{z,1}(\alpha) = 0.605 \sin(\alpha) + 0.0645 \quad (12)$$

where α is measured in radians. As shown in Fig. 4b, this model closely matches the recorded data and no significant variations due to wind speed or rotor speed are observed. $C_{z,1}$ can be seen to decrease as α decreases, becoming negative for $\alpha < -5^\circ$. This indicates that, while a small amount of lift force is generated when the UAV is close to horizontal, it is quickly overcome by frame drag, resulting in a net downward force applied along the $^B z$ axis.

The predicted F_{aero_z} using the above model was then further subtracted from the recorded z -axis force measurements. $C_{z,3}$ was then computed for all the available data. Similar to the previous coefficient, the function has to be even about $\alpha = 90^\circ, -90^\circ$. The following function was thus fitted to the experimental data using nonlinear least squares:

$$C_{z,3}(\alpha, \lambda_i) = 0.0645 \sin(\alpha) - 0.0207(1 - e^{-0.0536\lambda_i}) \sin(3\alpha) + 9.17 \times 10^{-3} \quad (13)$$

where

$$\lambda_i = \frac{\omega_i D_{\text{prop}}}{2U} \quad (14)$$

represents the rotors' tip speed ratio. Figure 4c shows that despite a rather large spread of the data, which is mostly due to data recorded at lower wind speeds, the main underlying trends of the data are captured. Similarly to $C_{z,1}$, $C_{z,3}$ changes from positive to negative with decreasing angles of attack. At small angles the thrust is enhanced, but as the angle becomes more negative the axial component of the wind has a negative effect. This agrees with findings from Khan and Nahon [15] and is consistent with theory as a higher axial inflow speed will reduce the thrust generated by a rotor. Figure 4d compares the total force measured along the z axis with the sum of the body axial force and all four rotor axial forces predicted by the above models. The total predicted force closely matches the experimental data at both $\alpha = 0^\circ$ and $\alpha = -45^\circ$, proving that despite the uncertainty in the $C_{z,3}$ data, the overall predicted force is accurate. Intermediate data omitted from the figure for the sake of clarity were found to fit equally well.

In a similar fashion, the transverse components of the aerodynamic and rotor forces are modeled as

$$F_{\text{aero}_x} = \frac{1}{2} \rho U^2 C_{x,1}(\alpha) A_{\text{UAV}} \quad (15)$$

$$T_{i_x} = \frac{1}{2} \rho C_{x,2}(\alpha, \lambda_i) U \omega_i D_{\text{prop}} A_{\text{prop}} \quad (16)$$

where $C_{x,1}$ and $C_{x,2}$ are dimensionless aerodynamic coefficients. Under the assumption that the UAV is symmetrical about its $^B x^B y$ plane, the functions for these coefficients must be even about $\alpha = 0^\circ$. In addition, they should be zero and odd about $\alpha = 90^\circ, -90^\circ$. $C_{x,1}$ was first computed for the data recorded at zero rotor speed. An empirically chosen model was then fitted to the resulting coefficients, yielding

$$C_{x,1}(\alpha) = 0.282 \cos(\alpha) - 0.0267 \cos(3\alpha) - 0.0145 \cos(7\alpha) \quad (17)$$

Figure 4e shows an acceptable fit. Decreasing α results in little $C_{x,1}$ variation, with a maximum deviation from the mean of approximately

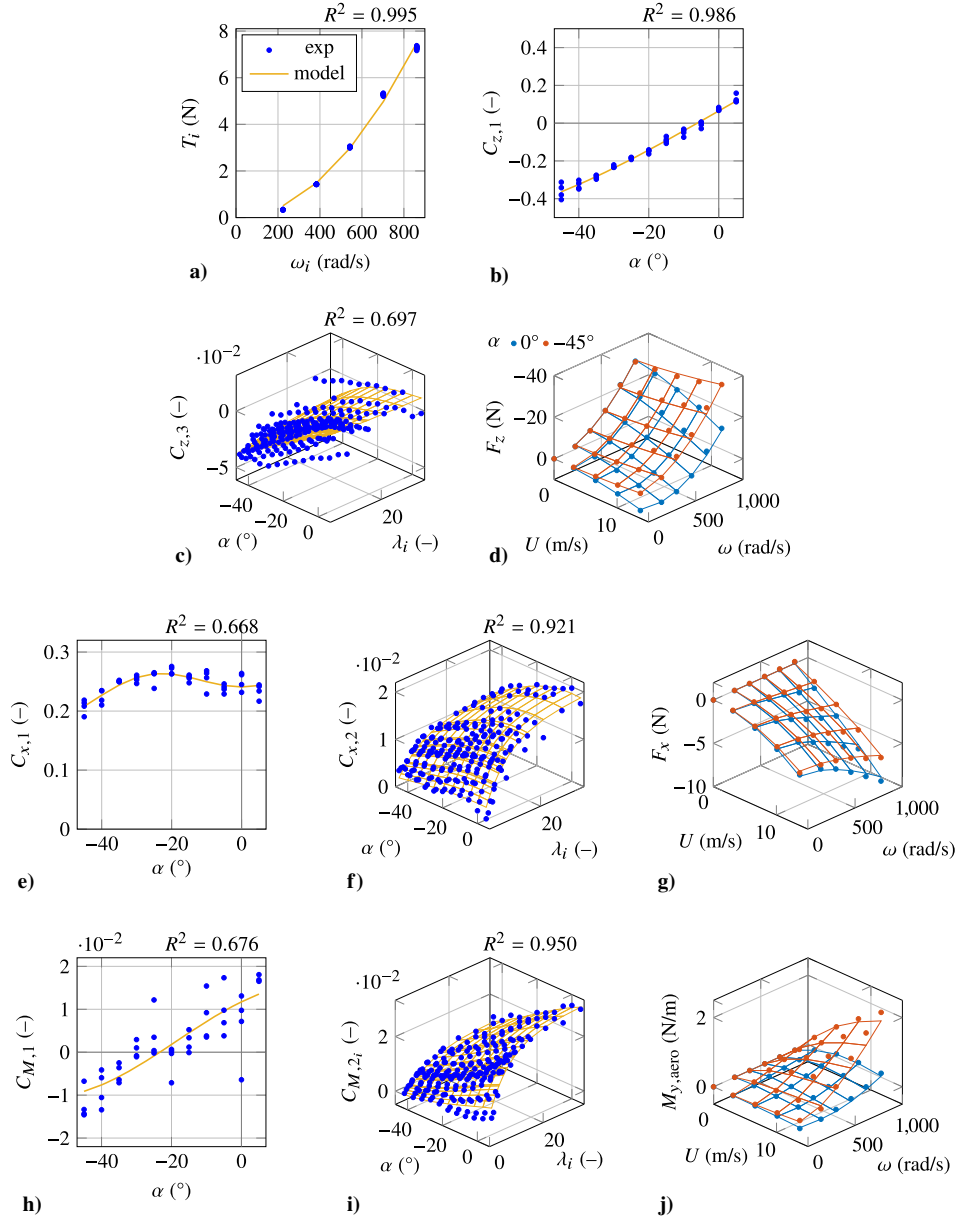


Fig. 4 Comparison of aerodynamic coefficients, forces, and moment with varying inflow angle α , rotor speed ω , and tip speed ratio λ_i . **a)** Individual rotor thrust; **b, c)** axial force coefficients; **e, f)** transverse force coefficients; **h, i)** moment coefficients; **d, g, j)** net aerodynamic forces and moment computed using the presented models (grids) against those measured in the experiment (dots).

$\pm 15\%$. This indicates that the sum of the components of drag and lift about the B_x axis stays relatively constant over the tested range of angles of attack.

The predicted $F_{aero,x}$ obtained using the above model was then subtracted from the recorded x -axis force measurements. The remainder was then used to compute the value of $C_{x,2}$ for each data point. As variations in α alone did not completely explain variations in coefficient, a function of both α and λ_i was then fitted, yielding

$$C_{x,2}(\alpha, \lambda_i) = 0.0175(1 - e^{-0.115\lambda_i}) \cos(\alpha) + 1.40 \times 10^{-3}(1 - e^{-0.266\lambda_i}) \cos(3\alpha) \quad (18)$$

Figure 4f shows a good match. $C_{x,2}$ can be seen to decrease as α becomes more negative. In addition, higher tip speed ratios are seen to correspond to higher $C_{x,2}$. As shown in Fig. 4g, the total x -axis force predicted by the above models follows the trends in the experiment.

The magnitude of the aerodynamic moment about the UAV's center of mass, $B_{M_{aero}}$, is modeled as

$$M_{aero} = \frac{1}{2} \rho U^2 C_{M,1}(\alpha) A_{UAV} D_{UAV} + \frac{1}{2} \rho U A_{prop} D_{prop}^2 \sum_{i=1}^N (\omega_i C_{M,2,i}(\alpha, \lambda_i)) \quad (19)$$

where $C_{M,1}$ and $C_{M,2,i}$ are dimensionless aerodynamic coefficients. The equations for these coefficients must be odd about $\alpha = 90^\circ$, -90° . The first term represents the aerodynamic moment acting on the body of the UAV, whereas the second term accounts for rotor aerodynamic moments.

For a typical symmetrically arranged UAV with identical propellers, no net moment is expected at zero wind speed. Any moment measured is thus due to rotor differences or misalignments due to the specific UAV used. To isolate aerodynamic effects, the y -axis moments measured were therefore zeroed at zero wind speed. In addition, the moments generated by $F_{aero,x}$ about the center of the sensor were subtracted from the zeroed y -axis moments. In a similar fashion to the axial force coefficients, a two-step procedure was then used to fit $C_{M,1}$ and $C_{M,2,i}$. $C_{M,1}$ was first computed for all y -axis

moment measurements taken at zero rotor speed. An empirically chosen sinusoidal-based model was then fitted to the resulting coefficients, yielding

$$C_{M,1}(\alpha) = 7.50 \times 10^{-3} \cos(\alpha) + 4.22 \times 10^{-3} \cos(3\alpha) + 0.0114 \sin(2\alpha) \quad (20)$$

As shown in Fig. 4h, the experimental data have a relatively large spread. However, the underlying trend of $C_{M,1}$ decreasing as α decreases was captured by the model. $C_{M,1}$ can be observed to become negative for $\alpha < -20^\circ$. This indicates that for α angles close to zero, the moment generated will try to make the UAV tilt upward. However, at more negative α angles the moment will make the UAV tilt further downward.

Using the model obtained for $C_{M,1}$, the moments resulting from the first term of M_{aero} were subtracted from all measured data in order to isolate moments due to rotor aerodynamic forces. Variations in α alone could not adequately explain the remaining moments. As a consequence, a more complex model dependent on both α and λ_i was used for $C_{M,2}$. The coefficient was first computed for all the data. Nonlinear least squares regression was then used to fit an empirically chosen model, yielding

$$C_{M,2}(\alpha, \lambda_i) = 0.0289(1 - e^{-0.127\lambda_i}) \cos(\alpha) + 9.77 \times 10^{-3}(1 - e^{-0.514\lambda_i}) \sin(2\alpha) \quad (21)$$

As shown in Fig. 4i, this function captures the trends of the experimental data well. Increasing the tip speed ratio λ_i is found to increase $C_{M,2}$, while decreasing α decreases $C_{M,2}$. Both these trends are consistent with findings from Khan and Nahon [15]. The quality of the fits is further proved in Fig. 4j, which shows a good fit between the total aerodynamic moment predicted by the above models and the moment measured in the experiment.

IV. Experimental Validation: Pitch Responses

The motivation behind this research is to develop a model suitable for the simulation of a hovering UAV in turbulent wind. Because the attitude of a UAV determines the direction of its net thrust vector, any motion of the craft will require a change in attitude. As a consequence, the angular response of a UAV is critical to flight performance. For a UAV model to be useful for tuning existing controllers and developing new controllers, it should therefore replicate the angular response trends observed on a real system. As the models introduced in the previous section were obtained from static data, they do not account for unsteady dynamics. The experiment conducted in this section thus aims to validate the dynamic angular response of the system by comparing simulated and experimental pitch responses. An existing flight controller using its default proportional–integral–derivative controllers is used for this experiment.

A. UAV Controller Description

The quadcopter presented in Sec. III is controlled by a Pixhawk flight controller running PX4 Pro Firmware v1.3 [25]. The flight control unit was chosen due to its common use in UAV research and available support libraries. The firmware was chosen due to its inbuilt support for motion capture pose feedback. No modifications were made to the controller and all controller settings were kept to their default values.

For the purpose of pitch response testing, the UAV was flown in manual stabilize mode. In this mode, the user manually provides the controller with reference roll, pitch, and yaw angles as well as a prescribed thrust. A simple proportional loop is applied to each axis to obtain desired angular velocities. The velocity loop for each axis uses a proportional–integral–derivative controller to yield desired motor commands.

B. Experimental Setup

The UAV was flown in an indoor environment in order to remove the influence of external wind. The UAV was controlled in manual mode by a pilot the entire time. The UAV started from a hover position. The pilot then sent a -5° pitch command to the UAV and flew in a straight line over a distance of 15 m while manually keeping the altitude constant. This yielded 7.5 s of usable flight data for each flight test. This experiment was repeated seven times. The UAV attitude and motor commands were logged to the onboard flight controller.

This testing methodology has a few limitations. First of all, due to the speed of the UAV a large amount of horizontal space was required, which made the use of motion capture impossible with the available equipment. As a consequence, a pilot had to manually control the UAV. To minimize the effects of human error, multiple runs were performed. The largest indoor flight area available was only 15 m long, which meant that only small pitch angle references could be safely provided. Second, the reference pitch signal was given by manually pushing an analog control stick to its limit as fast as possible. The angle corresponding to that limit was set in the transmitter's options. Because of the analog nature of the command, pure step commands could not be given; the rising edge was instead a steep slope.

C. Simulation Setup

The system equations of motion, motor, and drag models described in Secs. II and III were implemented in a simulation model using Simulink. In addition, copies of the PX4 stabilize controller, position hold controller, attitude estimator, and position estimator were also integrated within the simulation. In stabilize mode, the attitude is controlled by the stabilize controller, whereas the altitude has to be manually controlled through direct thrust commands by the operator. To replicate this behavior in simulation, the desired attitude commands recorded in the experimental tests were used as input to the attitude controller. In addition, a thrust controller composed of a PID controller and a feed-forward component compensating for gravity and wind-induced lift forces was implemented to simulate manual altitude control from a human pilot.

A 12.6 V power supply, corresponding to a fully charged three-cell battery, was used for the static tests. However, a voltage drop was observed when performing flight experiments using a real battery. The output of the transfer function between the PWM signal and ω was thus scaled by a factor of 0.84, which corresponds to the measured operating voltage of 10.7 V.

For comparison purposes, the pitch response of a simple UAV model that only models rotor thrust and ignores aerodynamic moments was also simulated. This was achieved by setting $C_{z,1} = C_{z,3} = C_{x,1} = C_{x,2} = C_{M,1} = C_{M,2} = 0$.

D. Results and Discussion

The seven step responses were each analyzed over a 7.5 s period. The average RMS pitch error was found to be 1.68° for the experiments and 1.16° in simulation using the presented aerodynamic models, or 31% lower. Likewise, the average peak error was 2.77° in experiments compared with 2.31° for the full simulation, or 17% lower. For comparison, the simulation model that does not model aerodynamic moments yielded a much lower average RMS error of 0.37° .

To investigate the source of these differences, a typical step response is shown in Fig. 5a. In accordance with the peak and RMS errors previously mentioned, the simulated response of the full system consistently shows a lower pitch error. In addition, it is less noisy than the experimental response. These differences can be explained by unmodeled dynamics, including structural vibrations, resulting in a higher amount of noise, and imperfections in the experimental setup that require manual yaw, roll, and thrust compensation. Because of the coupling between the different axes, these manual adjustments would decrease the pitch performance. However, both responses are seen to follow the same overall trends. They both initially track the reference signal in a similar fashion.

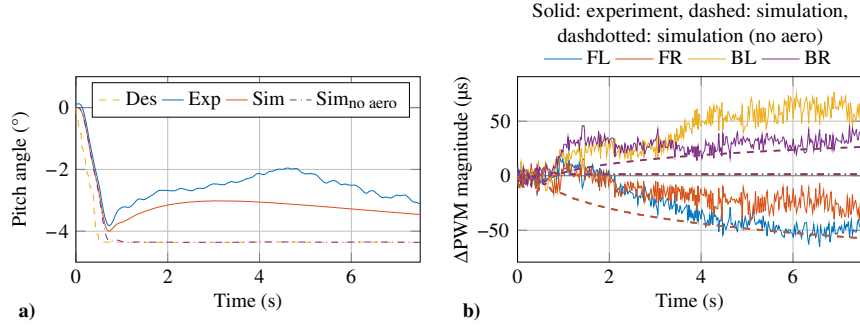


Fig. 5 Comparison of typical -5° step pitch responses for experimental and simulation systems, with and without the aerodynamic moment model. a) Pitch response; b) change in motor PWM compared with hover.

After around 0.7 s, the pitch error of the UAV starts increasing. This is expected because as the UAV pitches forward, it starts accelerating. As its relative speed increases, the aerodynamic moment applied on the UAV increases in accordance with Eq. (19). As the speed of the UAV approaches steady-state and the integrated error starts building up, the pitch error of the UAV starts to decrease again, as seen at around 3 s in the simulation response and 4 s in the experimental response. These trends can be confirmed by observing the PWM signals sent to the rotors, presented in Fig. 5b. Over the first 0.7 s there is little offset between signals sent to the front (FL and FR) and back (BL and BR) motors. After this point, the PWM signals sent to the front rotors can be seen to decrease, whereas the signals sent to the back rotors increase due to the integral component of the pitch control loop. On the other hand, the response of the system using the simpler aerodynamic model that does not model rotational aerodynamic moments is completely missing these trends. At first, the pitch response is similar to that of the full model. However, instead of increasing again after the 0.7 s mark, the pitch error is quickly driven to zero. Likewise, no PWM offset between the front and back rotors is observed. This indicates that the addition of the aerodynamic moment model enables to capture trends that are completely ignored by more widely used UAV models.

A limitation of the results presented here lies in the fact that the test area was not large enough for the pitch response to reach steady state. Because of the integral term in the angular velocity loop, a zero steady-state error is expected, as was found to be the case using the simulation model.

V. Experimental Validation: Hover in Turbulent Wind

To assess the usefulness of the simulation model derived previously to predict station-keeping performance, free flight station-keeping tests were performed in the University of Auckland's wind tunnel. This section describes the testing procedure followed and compares the experimental results to the results of a simulation of the UAV model described in the previous sections.

A. Experimental Setup

Figure 6 shows the wind tunnel. The exit walls of the wind tunnel were set 7 m apart. The nominal flight location of the UAV was



Fig. 6 Wind tunnel with grid.

located at an altitude of 1.5 m, 2.5 m away from the exit of the wind tunnel. A grid was added upstream of the UAV in order to generate a higher level of wind disturbance and shift more energy to lower frequencies to better replicate outdoor wind conditions.

Motion capture cameras were mounted in the flight area and the measured pose was streamed to the UAV's flight controller. The same flight control unit described in Sec. IV was used for this set of experiments. The PX4 "position hold" controller was used for both the simulations and the experiments.

B. Wind Tunnel Wind Speed Characterization

This section aims to present wind speed characteristics that are essential to the free flight test; a more thorough analysis of the wind tunnel is presented by the authors in [24]. Figure 7 shows the power spectral density (PSD) [26] of the wind measured along the x axis in the nominal flight location using a Cobra probe. In addition, PSDs obtained using a von Kármán wind turbulence model [26] are included. An altitude of 1.5 m and roughness length of 0.1 m were used for these PSDs, corresponding to an outdoor countryside environment with trees and hedges. The measured PSDs are relatively constant throughout the range of wind speeds used. Increasing the mean wind speed from 3.1 to 5.2 m/s results in a small increase in the frequency of the PSD peak from approximately 5 to 7.5 Hz. The peak frequency in an outdoor environment is typically between one and two orders of magnitude smaller than those obtained here, as can be seen in the PSDs obtained using the von Kármán model. As a consequence, differences between indoor and outdoor testing are to be expected. However, the extent of these differences is likely to be mitigated because UAVs are well suited to rejecting low-frequency disturbances. In the steady wind case, a UAV simply needs to pitch at the appropriate angle for the horizontal component of its thrust to match the horizontal component of the aerodynamic force acting on it. As long as the total thrust required is within the capabilities of the UAV, the lower the frequency of the wind disturbance, the closer from this steady state case and thus the easier it is for the UAV to station keep.

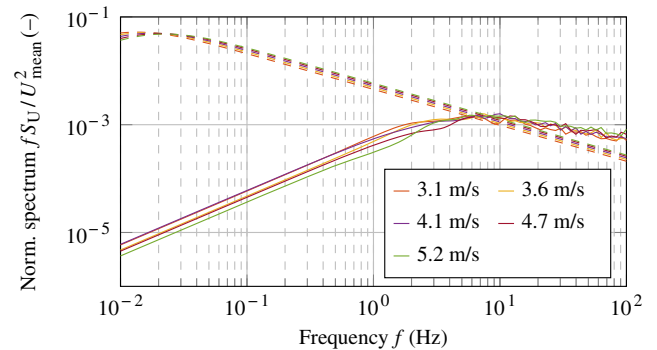


Fig. 7 Estimate of the PSD of the wind generated by each wind tunnel setting along the x axis. The dashed lines represent PSDs obtained from a von Kármán wind turbulence model.

Table 1 Wind characteristics measured using cobra probe

U_{mean} , m/s	Turbulence intensity, %		
	x	y	z
3.1	11.0	8.7	8.5
3.6	11.4	8.7	8.5
4.1	11.9	8.8	8.7
4.7	12.0	8.9	8.6
5.2	12.6	9.0	8.8

Table 1 shows the turbulence intensity of all three wind components. Turbulence intensity is defined as $TI_i = \sigma_i / U_{\text{mean}} \times 100\%$, $i \in \{x, y, z\}$, where σ_x represents the standard deviation of the wind speed around the x axis. The turbulence intensities can be seen to remain relatively stable across the whole range of mean wind speeds. In addition, the turbulence intensity across the x axis is seen to be between 30 and 40% higher than that across the y and z axes. On the other hand, the turbulence intensity is lower than that expected in an open countryside environment.

C. Simulation Setup

The same simulation model described in Sec. IV.C was used as a basis for flight experiments. In this case, both the position hold and attitude controllers were used in order to replicate the experimental testing conditions. Identical control gains and settings were used.

The wind profiles used as input to the aerodynamics models were obtained in three steps. First, a fast Fourier transform was applied to each wind time series recorded using the cobra probe. Then, frequency domain models were fitted to the data in each case. Finally, the fitted models were used with random seeds in order to generate 10-min-long wind profiles with similar characteristics to that originally measured in the wind tunnels. The wind speed profiles generated are only point profiles as spatial variations are assumed to be negligible.

D. Testing Procedure

The wind tunnel fan speed setting was varied over the range $\{3.1, 3.6, 4.1, 4.7, 5.2\}$ m/s. One 5 min flight test was performed for each wind speed setting. The UAV's pose and control signals were recorded on its on-board flight logs. The UAV was flown in the automatic "position hold" flight mode, yielding 2.5 min of usable flight data for each fan setting after cropping out data corresponding to the setup and landing of the UAV.

E. Results and Discussion

Figure 8 shows the position response obtained at the highest mean wind speed of 5.2 m/s in both the experimental test and the simulation. Visually, the x -axis response is similar between the experiment and simulation, showing evidence that the model is appropriate for simulating station-keeping performance. On the other hand, the z -axis and especially the y -axis responses exhibit lower peaks in simulation than in the experiment. An interesting observation is that in the experiment, the error responses for all three axes are similar in terms of amplitude even though the wind along the x axis was measured to have a higher turbulence intensity, as explained in Sec. V.B.

To investigate the station-keeping performance in more depth, Fig. 9 shows the standard deviation of the tracking error against wind speed for each axis. For all three axes the simulation tracking error has a zero mean. Despite experimental inaccuracies, the mean of the tracking error recorded in the experiment remains below 0.015 m across all axes and for all wind speeds. Barring an outlier for the y -axis error at a wind speed of 3.1 m/s in the experiment, the standard deviations of the error for both the experiment and simulation are seen to increase with increasing wind speed. This is expected as higher wind speeds result in disturbances of higher amplitude, which in turn negatively affect station-keeping performance. The mean x -axis standard deviation is on average 7%

higher in the simulation than in the experiment. The simulated and experimental x -axis standard deviations are thus close in magnitude, which matches what is observable on Fig. 8. On the other hand, the simulated standard deviations of the errors about the y and z axes are on average 43% and 56% lower than those found in the experiment, respectively.

To investigate the source of these differences, Fig. 10a shows the standard deviation of the UAV's attitude errors against wind speed. In addition, the mean pitch angle of the UAV is shown in Fig. 10b. A good match in mean pitch angle can be observed between the simulation and experimental results, which is expected as the aerodynamic models were obtained from static experiments. Slight differences between experimental and simulated mean pitch angles are seen to correspond with slight differences in roll angles, indicating that the x axis of the UAV was not perfectly aligned with the dominant wind direction. The standard deviation of the angular errors is seen to increase as wind speed increases, as shown in Fig. 10a. Furthermore, the standard deviation of the pitch angle errors is similar between the experiment and simulation, whereas the standard deviation of the simulated roll errors is larger than that of the experimental response. This is consistent with the position errors discussed previously. For example, a higher standard deviation of roll angles results in higher y -axis errors. Finally, a significant difference can be observed between the standard deviation of the yaw angle

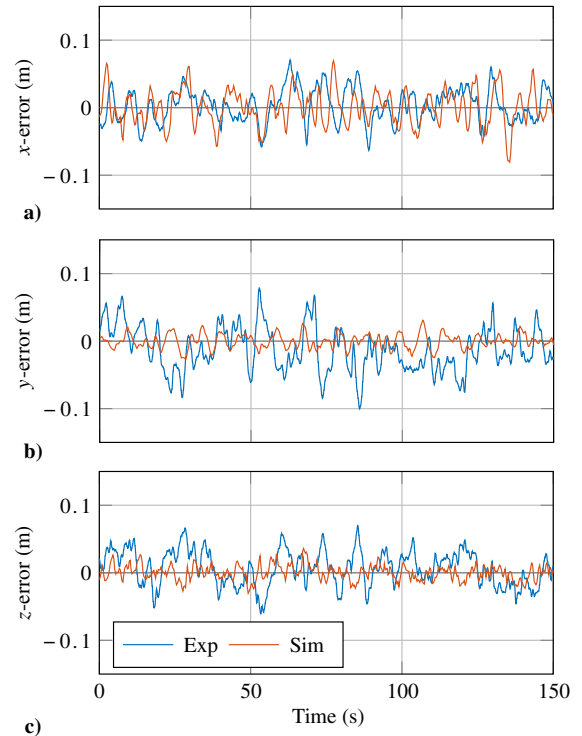


Fig. 8 Example station-keeping error responses for mean wind speed of 5.2 m/s over a 150 s period. a) Experiment; b) simulation.

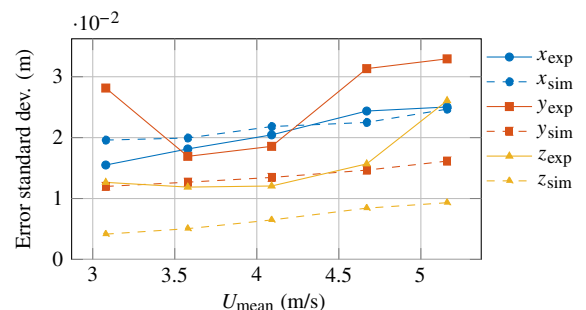


Fig. 9 Standard deviations of the position errors of the UAV in the world frame during station-keeping tests.

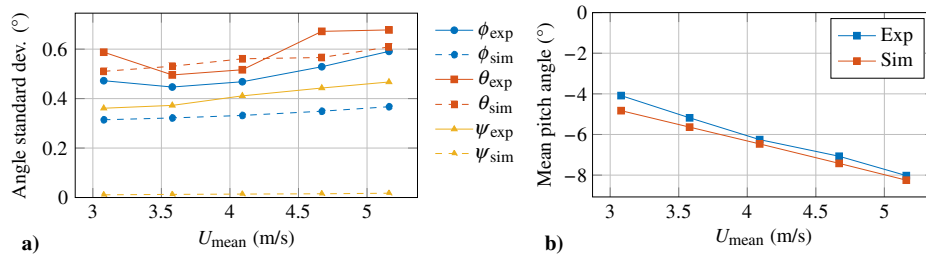


Fig. 10 UAV angles in simulation and experiment. a) Standard deviations; b) mean pitch.

errors between simulated and experimental results. This is explained by the fact that the model presented in this paper does not model imbalances, asymmetries, or rotational drag around the z axis. Furthermore, this difference in yaw angle error explains the discrepancy between the simulated and experimental y - and z -axis performance. In simulation, the standard deviation of yaw errors is insignificant across all wind speeds, whereas on the real system it is similar in magnitude to the standard deviation of the roll errors. Imperfect yaw regulation results in nonzero sideslip angles. In turn, this causes a component of the wind along the x axis to act along the y axis. Because the wind has a higher standard deviation along the x axis than along other axes, this reduces the roll performance and introduces coupling between the axes of the UAV. As a consequence, the station-keeping performance of the system decreases. A more complicated simulation model including aerodynamics yaw moments could be developed in order to provide more accurate results. However, the current model is deemed acceptable for the comparison of controller performance, as it is accurate along the x axis and captures the increasing trends along the y and z axes even though it underestimates the magnitude of the errors along those axes.

VI. Conclusions

Aerodynamic force, moment, and rotor thrust models based on static experimental data obtained in a wind-tunnel were created. Good parameter match for the chosen model forms was demonstrated. These models were integrated with a rigid-body UAV dynamics model and the open source PX4 position hold controller with the aim of creating a simulation model that could be used to assess controller performance for hover in turbulent wind. Step pitch response experiments were conducted to assess the quality of the models, showing simulated RMS pitch tracking errors within 31% on average of that obtained in the experiment and maximum pitch errors within 17% on average. Experimental validation of the entire system was performed using station-keeping experiments in a wind tunnel at various wind speeds. Good match was found along the dominant direction of the wind, the x axis, but the standard deviations of the errors along the y and z axes were found to be, respectively, 43% and 56% lower in simulation than in the experiment. However, similar trends were found between experimental and simulation results; in all cases the error spread was found to increase with increasing mean wind speed, making the model useful for comparing controller performance.

Improving the model presented in this paper would involve the addition of a three-dimensional wind field model, the modeling of aerodynamic yaw moment, and an investigation of transient aerodynamic effects in order to improve the predictive ability of the simulation model.

Acknowledgments

This research was made possible thanks to a University of Auckland Doctoral Scholarship and a Faculty Research Development Fund Grant. The authors thank the University of Auckland's Aerodynamics Laboratory staff for their help operating the wind tunnel and Nick Velychko in particular for providing the logging software used for the static experiments.

References

- [1] Kutia, J. R., Xu, W., and Stol, K. A., "Modeling and Characterization of a Canopy Sampling Aerial Manipulator," *2016 IEEE International Conference on Robotics and Biomimetics (ROBIO)*, IEEE Publ., Piscataway, NJ, 2016, pp. 679–684. doi:10.1109/ROBIO.2016.7866401
- [2] Nex, F., and Remondino, F., "UAV for 3D Mapping Applications: A Review," *Applied Geomatics*, Vol. 6, No. 1, 2014, pp. 1–15. doi:10.1007/s12518-013-0120-x
- [3] Faïçal, B. S., Pessin, G., Filho, G. P. R., Carvalho, A. C. P. L. F., Gomes, P. H., and Ueyama, J., "Fine-Tuning of UAV Control Rules for Spraying Pesticides on Crop Fields: An Approach for Dynamic Environments," *International Journal on Artificial Intelligence Tools*, Vol. 25, No. 1, 2016, pp. 1–19. doi:10.1142/S0218213016600034
- [4] Gremillion, G. M., and Humbert, J. S., "Disturbance Rejection with Distributed Acceleration Sensing for Small Unmanned Aircraft Systems," *AIAA Journal*, Vol. 54, No. 8, 2016, pp. 2233–2246. doi:10.2514/1.J054408
- [5] Artale, V., Milazzo, C. L. R., and Ricciardello, A., "Mathematical Modeling of Hexacopter," *Applied Mathematical Sciences*, Vol. 7, No. 97, 2013, pp. 4805–4811. doi:10.12988/ams.2013.37385
- [6] Bresciani, T., "Modelling, Identification and Control of a Quadrotor Helicopter," Master's Thesis, Lund Univ., Lund, Sweden, Aug. 2008, <http://lup.lub.lu.se/student-papers/record/8847641> [retrieved 28 Sept. 2018].
- [7] Luukkainen, T., "Modelling and Control of Quadcopter," *Independent Research Project in Applied Mathematics*, Aalto Univ., Espoo, Finland, Aug. 2011, p. 4, http://sal.aalto.fi/publications/pdf-files/eluu11_public.pdf [retrieved 28 Sept. 2018].
- [8] Benić, Z., Piljek, P., and Kotarski, D., "Mathematical Modelling of Unmanned Aerial Vehicles with Four Rotors," *Interdisciplinary Description of Complex Systems*, Vol. 14, No. 1, 2016, pp. 88–100. doi:10.7906/index.14.1.9
- [9] Cabecinhas, D., Cunha, R., and Silvestre, C., "A Globally Stabilizing Path Following Controller for Rotorcraft with Wind Disturbance Rejection," *IEEE Transactions on Control Systems Technology*, Vol. 23, No. 2, 2015, pp. 708–714. doi:10.1109/TCST.2014.2326820
- [10] Sydney, N., Smyth, B., and Paley, D. A., "Dynamic Control of Autonomous Quadrotor Flight in an Estimated Wind Field," *Proceedings of the 52nd Annual Conference on Decision and Control*, IEEE Publ., Piscataway, NJ, 2013, pp. 3609–3616. doi:10.1109/CDC.2013.6760438
- [11] Månsson, C., and Stenberg, D., "Model-Based Design Development and Control of a Wind Resistant Multirotor UAV," Master's Thesis, Lund Univ., Lund, Sweden, 2014, <http://lup.lub.lu.se/student-papers/record/4610294> [retrieved 28 Sept. 2018].
- [12] Ramasamy, M., "Hover Performance Measurements Toward Understanding Aerodynamic Interference in Coaxial, Tandem, and Tilt Rotors," *Journal of the American Helicopter Society*, Vol. 60, No. 3, 2015, pp. 1–17. doi:10.4050/JAHS.60.032005
- [13] Yoon, S., Chan, W. M., and Pulliam, T. H., "Computations of Torque-Balanced Coaxial Rotor Flows," *Proceedings of the AIAA SCITECH Forum 2017*, AIAA Paper 2017-0052, 2017, pp. 1–12. doi:10.2514/6.2017-0052
- [14] Theys, B., Dimitriadis, G., Andrianne, T., Hendrick, P., and De Schutter, J., "Wind Tunnel Testing of a VTOL MAV Propeller in Tilted Operating Mode," *2014 International Conference on Unmanned Aircraft Systems (ICUAS)*, IEEE Publ., Piscataway, NJ, 2014, pp. 1064–1072. doi:10.1109/ICUAS.2014.6842358
- [15] Khan, W., and Nahon, M., "A Propeller Model for General Forward Flight Conditions," *International Journal of Intelligent Unmanned*

- Systems*, Vol. 3, Nos. 2/3, 2015, pp. 72–92.
doi:10.1108/IJUS-06-2015-0007
- [16] Tran, N. K., Bulka, E., and Nahon, M., “Quadrotor Control in a Wind Field,” *2015 International Conference on Unmanned Aircraft Systems (ICUAS)*, IEEE Publ., Piscataway, NJ, 2015, pp. 320–328.
doi:10.1109/ICUAS.2015.7152306
- [17] Luo, J., Zhu, L., and Yan, G., “Novel Quadrotor Forward-Flight Model Based on Wake Interference,” *AIAA Journal*, Vol. 53, No. 12, 2015, pp. 3522–3533.
doi:10.2514/1.J053011
- [18] Bannwarth, J. X. J., Chen, Z. J., Stol, K. A., and MacDonald, B. A., “Disturbance Accommodation Control for Wind Rejection of a Quadcopter,” *2016 International Conference on Unmanned Aircraft Systems (ICUAS)*, IEEE Publ., Piscataway, NJ, 2016, pp. 695–701.
doi:10.1109/ICUAS.2016.7502632
- [19] Suárez Fernández, R. A., Dominguez, S., and Campoy, P., “L1 Adaptive Control for Wind Gust Rejection in Quad-Rotor UAV Wind Turbine Inspection,” *2017 International Conference on Unmanned Aircraft Systems (ICUAS)*, IEEE Publ., Piscataway, NJ, 2017, pp. 1840–1849.
doi:10.1109/ICUAS.2017.7991485
- [20] Smeur, E. J. J., de Croon, G. C. H. E., and Chu, Q., “Gust Disturbance Alleviation with Incremental Nonlinear Dynamic Inversion,” *2016 IEEE/RSJ International Conference on Intelligent Robots and Systems (IROS)*, IEEE Publ., Piscataway, NJ, 2016, pp. 5626–5631.
doi:10.1109/IROS.2016.7759827
- [21] Lee, D.-K., and Han, J.-H., “Safety-Guaranteed Flight Test Environment for Micro Air Vehicles,” *AIAA Journal*, Vol. 54, No. 3, 2016, pp. 1018–1029.
doi:10.2514/1.J054241
- [22] Smeur, E. J. J., de Croon, G. C. H. E., and Chu, Q., “Cascaded Incremental Nonlinear Dynamic Inversion for MAV Disturbance Rejection,” *Control Engineering Practice*, Vol. 73, March 2018, pp. 79–90.
doi:10.1016/j.conengprac.2018.01.003
- [23] DJI, “DJI Flame Wheel ARF Kit,” 2018, <https://www.dji.com/flame-wheel-arf> [retrieved 28 Sept. 2018].
- [24] Bannwarth, J. X. J., Chen, Z. J., Stol, K. A., MacDonald, B. A., and Richards, P. J., “Development of a Wind Tunnel Experimental Setup for Testing Multirotor Unmanned Aerial Vehicles in Turbulent Conditions,” *2018 IEEE/ASME International Conference on Advanced Intelligent Mechatronics (AIM)*, IEEE Publ., Piscataway, NJ, 2018.
- [25] PX4 Dev Team, “Open Source for Drones—PX4 Pro Open Source Autopilot,” 2018, <http://px4.io/> [retrieved 28 Sept. 2018].
- [26] Burton, T., Jenkins, N., Sharpe, D., and Bossanyi, E., *Wind Energy Handbook*, 2nd ed., Wiley, Chichester, U.K., 2011, pp. 9–21.
doi:10.1002/9781119992714

C. Wen
Associate Editor